PCCP

ROYAL SOCIETY OF CHEMISTRY

PERSPECTIVE

View Article Online
View Journal | View Issue

Cite this: *Phys. Chem. Chem. Phys.*, 2022, **24**, 11471

Multimodal electrochemistry coupled microcalorimetric and X-ray probing of the capacity fade mechanisms of Nickel rich NMC – progress and outlook†

Calvin D. Quilty,‡[ab] Patrick J. West,‡[bc] Wenzao Li,‡[ab] Mikaela R. Dunkin,[bc] Garrett P. Wheeler,[bd] Steven Ehrlich,[e] Lu Ma,[e] Cherno Jaye,[f] Daniel A. Fischer,[f] Esther S. Takeuchi,[abcd] Kenneth J. Takeuchi,[abcd] David C. Bock *[bd] and Amy C. Marschilok *[abcd]

Lithium nickel manganese cobalt oxide (NMC) is a commercially successful Li-ion battery cathode due to its high energy density; however, its delivered capacity must be intentionally limited to achieve capacity retention over extended cycling. To design next-generation NMC batteries with longer life and higher capacity the origins of high potential capacity fade must be understood. *Operando* hard X-ray characterization techniques are critical for this endeavor as they allow the acquisition of information about the evolution of structure, oxidation state, and coordination environment of NMC as the material (de)lithiates in a functional battery. This perspective outlines recent developments in the elucidation of capacity fade mechanisms in NMC through hard X-ray probes, surface sensitive soft X-ray characterization, and isothermal microcalorimetry. A case study on the effect of charging potential on NMC811 over extended cycling is presented to illustrate the benefits of these approaches. The results showed that charging to 4.7 V leads to higher delivered capacity, but much greater fade as compared to charging to 4.3 V. *Operando* XRD and SEM results indicated that particle fracture from increased structural distortions at >4.3 V was a contributor to capacity fade. *Operando* hard XAS revealed significant Ni and Co redox during cycling as well as a Jahn–Teller distortion at the discharged state (Ni^{3+}); however, minimal differences were observed between the cells charged to 4.3 and 4.7 V. Additional XAS analyses using soft X-rays revealed significant surface reconstruction after cycling to 4.7 V, revealing another contribution to fade. *Operando* isothermal microcalorimetry (IMC) indicated that the high voltage charge to 4.7 V resulted in a doubling of the heat dissipation when compared to charging to 4.3 V. A lowered chemical-to-electrical energy conversion efficiency due to thermal energy waste was observed, providing a complementary characterization of electrochemical degradation. The work demonstrates the utility of multi-modal X-ray and microcalorimetric approaches to understand the causes of capacity fade in lithium-ion batteries with Ni-rich NMC.

Received 20th November 2021,
Accepted 6th April 2022

DOI: 10.1039/d1cp05254c

rsc.li/pccp

1 Introduction

1.1 NMC as a Li-ion battery cathode

Lithium nickel manganese cobalt oxide ($LiNi_xMn_yCo_zO_2$, NMC) is an important lithium-ion battery cathode material for electric vehicle applications due to its high capacity retention and high energy density.[1–8] NMC can be described as a layered, ordered rock salt that crystallizes in a hexagonal unit cell characterized by alternating layers of octahedrally coordinated lithium and nickel/manganese/cobalt where the transition metals all share

[a] *Department of Chemistry, State University of New York at Stony Brook, Stony Brook, New York 11794, USA. E-mail: amy.marschilok@stonybrook.edu*
[b] *Institute for Electrochemically Stored Energy, State University of New York at Stony Brook, Stony Brook, New York 11794, USA*
[c] *Department of Materials Science and Chemical Engineering, State University of New York at Stony Brook, Stony Brook, New York 11794, USA*
[d] *Interdisciplinary Science Department, Brookhaven National Laboratory, Upton, New York 11973, USA. E-mail: dbock@bnl.gov*
[e] *National Synchrotron Light Source II, Brookhaven National Laboratory, Upton, New York 11973, USA*
[f] *Material Measurement Laboratory, National Institute of Standards and Technology, Gaithersburg, Maryland 20899, USA*

† Electronic supplementary information (ESI) available: The supplemental information includes galvanostatic cycling curves, XRD patterns, hard and soft XAS spectra, XANES and EXAFS fitting results, and isothermal microcalorimetry data. See DOI: https://doi.org/10.1039/d1cp05254c

‡ Equivalent contributions.

one crystallographic site.[2,3,9] The three ions have distinct oxidation states where Ni is either 2+ or 2+/3+ depending on stoichiometry, Mn is 4+, and Co is 3+.[4,6,7] The nomenclature for NMC commonly follows the stoichiometric ratios of the three transition metals. For example, $LiNi_{0.33}Mn_{0.33}Co_{0.33}O_2$ and $LiNi_{0.8}Mn_{0.1}Co_{0.1}O_2$ are referred to as NMC111 and NMC811, respectively.

The properties of NMC can be optimized by adjusting the compositional ratio of the Ni, Mn, and Co in the material. Ni contributes to the higher cathode discharge capacity through greater Li (de)insertion within a defined voltage window; Co enhances the material's rate capability and stabilizes the layered structure of the cathode for long cycle life; Mn supports the electrochemical stability and thermal stability of the material for improved safety.[4,6,10–12] A large field of research focuses on manipulating the stoichiometric ratios of Ni, Mn, and Co to tune electrochemical performance. Indeed, Fig. 1[3,5,6,13–16] shows the recent dramatic increase in publications involving NMC materials. With a push to satisfy the higher energy density requirements necessitated by electric vehicles, significant attention has been given to Ni rich NMC compositions where $x > 0.5$; in these structures the nickel is a mixture of Ni^{2+} and Ni^{3+} where Ni^{3+} content increases with x. Ni rich NMC offers higher energy density as the high Ni content leads to greater lithium extraction.[4,6] In particular, NMC811 is of interest due to its exceptionally high energy density ($\sim$195 mA h g^{-1} compared to $\sim$160 for NMC111).[6,13–15,17–21] However, the high nickel content NMCs lack the stability of their Ni deficient analogs and present unique structural and electrochemical phenomena that require a large breadth of experimental techniques for full characterization.[12,18,20–22]

During charge, lithium is removed from the NMC crystallographic structure resulting in an initial contraction along the a axis and expansion along the c axis. However, at higher levels of delithiation ($>$0.67 electron equivalent), a dramatic contraction along the c axis is also observed.[2,3,13,14] Concurrently, nickel is oxidized to Ni^{3+} followed by Ni^{4+} and Co is oxidized to Co^{4+}; the oxidation state of Mn remains unchanged throughout cycling.[4,6,7] The Co–O bonds of CoO_6 octahedra uniformly contract from $\approx$1.92 Å to 1.88 Å as Co oxidizes from 3+ to 4+.[4,23–27]

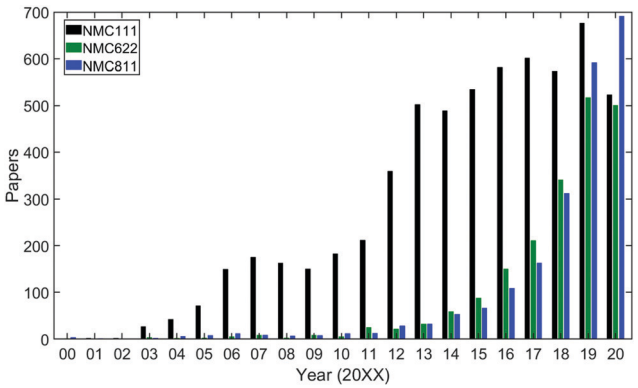

Fig. 1 Papers by year for NMC111, NMC622, and NMC811 from 2000–2020 from SciFinder Scholar search dated September 3rd, 2021.

Similarly, the NiO_6 octahedra also contract as nickel is oxidized to Ni^{4+} ($\approx$1.99 Å to 1.88 Å); however, this contraction is nonuniform.[4,23–27] Ni^{3+} is a low spin d^7 ion and as such is susceptible to Jahn–Teller distortions, so in the 3+ state, nickel is coordinated to four oxide ions at $\approx$1.91 Å and two at $\approx$2.09 Å.[4,23–27] Once charged, the NiO_6 octahedron becomes uniform and all six oxide ions are $\approx$1.88 Å for Ni^{4+} (Fig. 2).[4,23–27] It is important to note that local Jahn–Teller distortions can be transient and may not translate to sustained changes in the material's bulk structure – for example in the case of $LiNiO_2$ while Jahn–Teller distortions are seen locally, the global crystallographic symmetry is systematically identified as a perfectly undistorted rhombohedral structure isostructural with $LiCoO_2$.[28] However, electrochemically induced Jahn–Teller distortions which are repeated and/or persist during (de)lithiation can contribute to lasting impacts on the crystallographic integrity of electroactive materials.

Theoretically, NMC811 can deliver 275 mA h g^{-1} (1 electron equivalent) when fully delithiated; however, the delithiated structure is not stable and so delithiation must be limited to $\approx$67%, leading to a proportional reduction in delivered capacity.[29,30] Practically, this limitation can be employed by limiting the charging potential to $\approx$4.3 V.[13,14,29] It is of interest to charge NMC811 to higher potential as this will deliver more capacity. However, again, greater delithiation prompts structural instability which can result in loss of capacity over extended cycling.[13,29,31] Moreover, the degradation of the NMC811 material due to high voltage charge to 4.7 V may also result in additional heat generation. In a previous isothermal microcalorimetric study on $LiNi_{0.6}Mn_{0.2}Co_{0.2}O_2$ (NMC622),[32] charging to high voltage resulted in irreversible energy conversion from chemical energy to heat. The increased thermal output not only wastes energy but is also a potential safety hazard. There are many interrelated electronic and physical properties that influence NMC's electrochemical performance including but not limited to: chemical composition, transition metal oxidation state, metal-ligand coordination, local atomic arrangement, crystallinity, and even electrode structural integrity. These properties span a multitude of different length scales making identifying and employing appropriate techniques of great importance to understand NMC's electrochemical behavior. Using NMC811 as a model material, this perspective discusses common degradation mechanisms in NMC and how they can be elucidated using cutting edge electrochemistry coupled isothermal microcalorimetry (IMC) and X-ray characterization techniques.

1.2 Hard and soft X-rays as absorption spectroscopy probes

It is worthwhile to briefly consider the differences between absorption spectroscopy performed with hard & soft X-rays especially as these differences can lead to surface sensitivity for soft X-rays. Hard X-ray absorption spectroscopy (XAS) techniques probe the metal K-edge of transition metals where core-shell electrons are excited to the outer shell p orbitals ($1s^2$ to $1s^14p^1$) (Fig. 3). Oxidation state and electronic structure information are obtained through analysis of the X-ray absorption near edge structure (XANES) region, while details of the

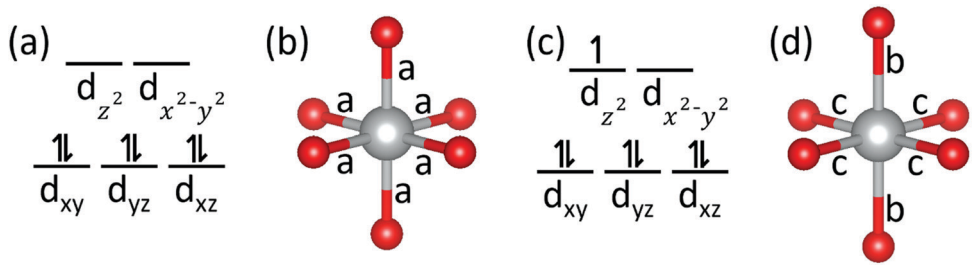

Fig. 2 (a) d-Orbital splitting diagram of Ni^{4+}, (b) coordination environment of Ni^{4+} (a = 1.88 Å), (c) d-orbital splitting diagram of Ni^{3+}, (d) coordination environment of Ni^{3+} (b = 2.09 Å, c = 1.91 Å).

local atomic environment including bond lengths and coordination number are obtained from the extended X-ray absorption fine structure (EXAFS) region. The high energies (>6 keV) required for K-edge excitation of Ni, Mn, and Co in NMC materials enable penetration through tens of micrometers of sample thickness, essentially meaning that the entirety of the sample is probed.

On the other hand, soft XAS targets the L-edge of transition metals wherein a 2p orbital electron is excited to the 3d valence holes ($2p^63d^n \rightarrow 2p^53d^{n+1}$).[33] After excitation, the remaining electrons in the $2s^5$ state split due to spin-orbital coupling giving rise to the L_3-edge ($2p_{J=3/2}$) and the L_2-edge ($2p_{J=1/2}$) in a theoretical ratio of 2 : 1.[34] Moreover, if the d^n orbital is partially filled, as is the case for transition metals, then the $2p^63d^n \rightarrow 2p^53d^{n+1}$ excitation is highly dependent on the initial electron state. Differences in oxidation state, electron spin-state, coordination, and crystal field strength all produce deviations in the L_3 and L_2-edges.[35] Each of these four factors manifest differently for different elements in different environments. Additionally, soft XAS can parse changes in valence state as a function of depth with different detection modes: partial electron yield (PEY, 1 nm to 2 nm), total electron yield (TEY, ≈5 nm) and fluorescence yield (FY, ≈50 nm to 100 nm).[5,36] Therefore, soft XAS has surface sensitivity and can be used to probe the electronic structure of the target element at the particle surface.

As an important point of clarification, the difference in energies between the L and K-edges of transition metals determines the use of hard or soft X-rays, respectively. But that is not the case for all elements. The O K-edge, for example, has an edge energy of 537 eV,[37] and therefore is collected *via* soft XAS measurement.

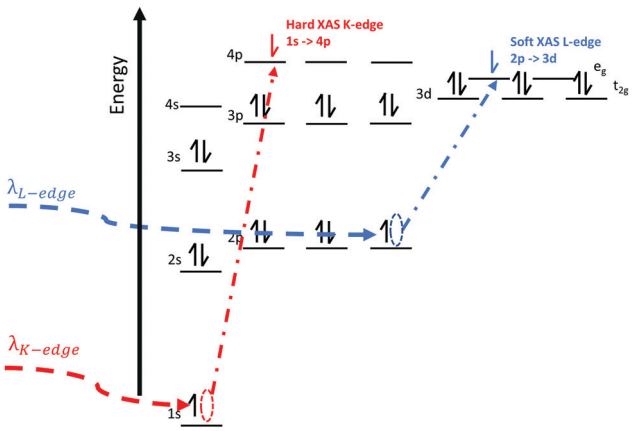

Fig. 3 Schematic of a low-spin Ni^{4+} ion's atomic orbitals during excitation due to hard X-rays (red) and soft X-rays (blue).

1.3 Applications of hard X-ray characterization towards elucidating capacity fade mechanisms

Hard X-ray characterization has proven essential for elucidating capacity fade mechanisms in Ni-rich NMC materials.[3–6,13,14,38–41] In particular, significant advances have been made characterizing these materials using X-ray diffraction (XRD) and hard XAS techniques.[3–6,13,14,23,38–42] Implementation of these techniques using *operando* methodology, where measurements are performed during battery operation,[3,4] enables the acquisition of relevant oxidation state, local atomic environment and crystal structure information without introducing the various artifacts associated with stopping and deconstructing the cell for *ex situ* measurement.[43] By performing these *operando* X-ray measurements on cells that have been extensively cycled, important insights into the mechanism of capacity fade can be obtained while that fade is actually occurring. To this end, extensively pre-cycled NMC622 cells have been studied with *operando* XRD, *operando* XAS, and combined XRD/XAS.[2–4] *Operando* XRD has also been applied to extensively cycled $LiNi_{0.91}Mn_{0.03}Co_{0.06}O_2$, $LiNi_{0.85}Mn_{0.05}Co_{0.1}O_2$, and NMC811 cells.[17,40,41,44]

Capacity fade due to structural instability is a significant problem for NMC811, particularly at high charging potential.[13,17,29,31] Upon delithiation, the material undergoes anisotropic lattice changes, where there is initially a small drop in cell volume upon moderate delithiation and then a more drastic drop in volume upon additional delithiation; this additional delithiation occurs when charged to high potential.[2,3,13,14,17,21] These repeated changes in the host lattice induce stress on the particles which can lead to cracking which induces capacity fade by degrading the electrical connection in the electrode.[14,17,19–21,29–31,45–47] For example, *operando* XRD measurements of Li/NMC811 half cells showed a 5.1% volumetric change of NMC811 when cycled between 3.0 V and 4.3 V, with increased microstrain correlated with microcracking of particles observed by scanning electron microscopy analysis.[14] Particle cracking can also lead to transition metal dissolution due to the increased surface area formed by the cracks.[2,48] This dissolution results in loss of active material and can lead to deposits on the anode which may be detrimental to performance.[2,7,20]

While hard X-ray characterization has proven critical for studying the NMC system; fundamentally these techniques provide bulk material information due to the high energy of hard X-rays, with sampling depths on order of tens of micrometers. As will be discussed in the next section, the surface of NMC also plays a critical role in capacity fading; soft XAS measurements with detection mode dependent sampling depths ranging from (1 nm to 2 nm) to (50 nm to 100 nm) can be used to unravel these non-bulk contributions.

1.4 Soft X-ray absorption spectroscopy (sXAS) as a surface sensitive probe for the determination of non-bulk fading mechanisms

Another potential factor causing capacity fade in NMC materials is surface reconstruction.[6] This phenomenon is spurred by repeated (de)lithiation events and results in the reconstruction of the NMC layered rhombohedral ($R\bar{3}m$) phase to cubic spinel ($Fd\bar{3}m$) and rocksalt ($Fm\bar{3}m$) phases at the particle surface (Fig. 4).[3,4,6,49] The decrease in oxide coordination number during delithiation can encourage oxygen liberation from the crystal structure, which triggers a conversion to the oxygen deficient spinel and rock salt phases,[6,12,17,19,20,31,50] The oxygen deficient phases tend to be less ionically conductive than the layered NMC parent, leading to impedance buildup and increased polarization which reduce electrochemical reversibility.[6,7,17,20] Additionally, the surface reconstruction phases also tend to be more soluble in carbonate-based electrolytes, which leads to active material dissolution & deposition on the adjacent anode, causing further fade.[7,20]

There have been limited reports providing physical evidence of surface reconstruction using bulk measurements. For example, Bak *et al.* performed *in situ* XRD on previously delithiated NMC433, NMC532, NMC622, and NMC811 materials that were heated to 600 °C.[12] The authors showed the formation of spinel and rocksalt NMC phases which formed at relatively lower temperatures for materials with higher Ni content. Critically, these phases could only be detected at the bulk level after significant heating. However, for NMC materials cycled at ambient temperatures and conditions, reconstruction is a primarily surface phenomenon and cannot be detected with bulk sensitive hard X-rays. Alternatively, M. Doeff and coworkers have shown that surface sensitive soft XAS analysis is a powerful tool for the detection of surface reconstruction phases in NMC materials of various compositions.[5,6,49] These studies have demonstrated that while Ni and Co undergo reversible redox on the bulk level during (dis)charge, there can be irreversible reduction of Ni, Mn, and Co in the first ≈10 nm of the NMC particles,[5,6,49] providing direct evidence of reduced surface phases that form during electrochemical cycling.

1.5 X-ray imaging

In addition to the use of XRD and XAS to track the crystallographic, oxidation state and local atomic structure changes associated with capacity fade, X-ray imaging techniques can be used to further probe aging mechanisms in NMC materials by enabling 3-dimensional characterization of microstructural and phase heterogeneities. One such imaging technique is X-ray computed tomography (CT). In conventional absorption contrast CT, X-rays are transmitted through a sample where differences in X-ray absorption from different sample components are used to provide image contrast. The technique can be used to quantify both electrode and particle level degradation in NMC electrodes.[20] A related technique to conventional CT is X-ray diffraction computed tomography (XRD-CT),[53] where image contrast is alternatively provided by differences in scattered X-rays from the sample components. This approach enables spatial localization of diffraction information and thus quantification of (de)lithiated phase heterogeneity at the electrode scale.[54–56] Recently, the first application of XRD-CT to NMC electrodes was used to analyze electrodes cycled under different voltage limits.[56] The results revealing more severe unit cell volume shrinkage for particles charged to higher voltage, consistent with a higher degree of active Li loss, and provided demonstration that XRD-CT can be an effective technique for

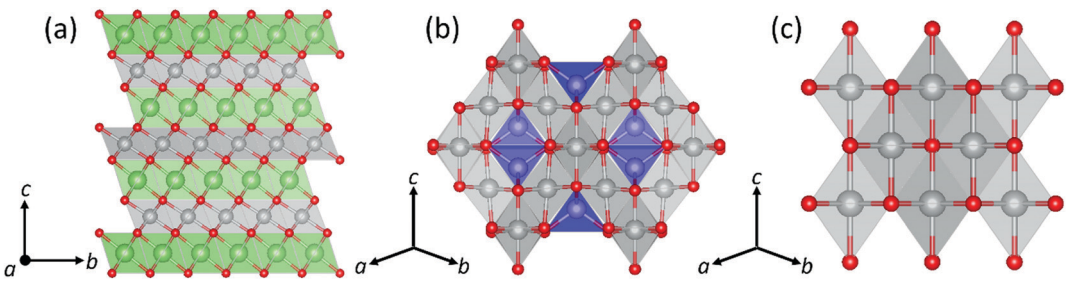

	(a)	(b)	(c)
Formula	$LiNi_{0.8}Mn_{0.1}Co_{0.1}O_2$	$(Ni_{0.8}Mn_{0.1}Co_{0.1})_3O_4$	$Ni_{0.8}Mn_{0.1}Co_{0.1}O$
S.G.	$R\bar{3}m$	$Fd\bar{3}m$	$Fm\bar{3}m$
TM charge	3+	2.67+	2+
O:TM ratio	2	1.33	1

Fig. 4 Schematic of the crystal structures, average transition metal charges, and oxygen to transition metal ratios of (a) layered NMC811,[9] (b) spinel,[51] and (c) rocksalt.[52] Lithium, transition metal, and oxide ions are colored green, gray, and red respectively. The tetrahedral site of the spinel (b) is noted in blue.

future studies aimed at understanding capacity fade in the material.[56]

A second X-ray imaging technique is transmission X-ray microscopy (TXM), which also uses X-ray absorption to provide image contrast, but which has higher resolution (tens of nanometers) and lower field of view (tens of microns) compared to conventional CT.[57] TXM has been used to detect cracking in secondary particles of NMC materials induced by electrochemical cycling.[21,58,59] In one notable example, TXM provided evidence of an electrode depth dependence on particle fracture, where mechanical failure is more severe in active materials near to the separator.[21] An additional advantage of TXM is that the XANES region of the sample can be obtained by scanning the incident X-ray energy across component element's X-ray absorption edge, thus enabling chemical state information as a function of spatial location. Using this approach, TXM has been used to quantify oxidation state heterogeneity in polycrystalline NMC secondary particles,[60,61] and has indicated that the alignment of the primary grains plays a critical role in determining cell polarization and capacity retention.[61]

1.6 Case study: capacity fade as a function of charge potential in NMC811

To highlight the importance of multimodal X-ray characterization for elucidating mechanisms contributing to capacity fade, this section presents a case study on NMC811. Specifically, this study aims to elucidate the various factors that lead to capacity fade as a function of charging potential; to this end, cells were cycled either from 3.0 V to 4.3 V or 3.0 V to 4.7 V. *Operando* XRD and XAS measurements were performed on Li/NMC811 cells before and after 100× cycling under those potential windows, providing direct measurements of oxidation state, local atomic environment, and crystal structure as fade progresses. sXAS measurements were performed to detect differences in the level of surface reconstruction that were invisible to the hard X-ray measurements. Additionally, *operando* isothermal microcalorimetry was performed to understand how charging voltage impacts thermal energy waste within the battery. The case study illustrates that a combined approach is needed to fully understand the factors leading to capacity fade in Ni-rich NMC.

2 Results and discussion

2.1 Electrochemistry

To study the origins of capacity fading at high charging potentials in NMC811, a 2 × 2 matrix of Li/NMC811 cells was considered. Cells that were uncycled and cells that were cycled 100× from either (3 to 4.3) V or (3 to 4.7) V were studied using *operando* techniques at the same potential windows; these cells are designated as 4.3 fresh, 4.7 fresh, 4.3 cycled, and 4.7 cycled.

When charged to 4.7 V, the NMC811 initially delivers 14% higher capacity than when charged to 4.3 V (Fig. 5A and B); consistent with the higher potential leading to greater delithiation. However, the (3 to 4.7) V cells fade significantly faster; the initial increased capacity is no longer observed by cycle 35, and after cycle 100 the (3 to 4.7) V cells lose 30% of their initial capacity compared to only 10% when cycled from 3 V to 4.3 V. It should be noted that the electrochemistry is comparable in both coin and pouch cells demonstrating the reproducibility independent of cell format. When charged (Fig. S1 and S2, ESI†), two plateaus are observed: the first at ≈3.7 V and the second smaller plateau at ≈4.2 V, followed by a steep increase in potential with no notable features. These plateaus are observed upon discharge as well; but they become much less defined after cycling. After 100 cycles, a significant increase in impedance is observed, where the increase is more pronounced for the cell charged to the higher potential (Fig. 5C).

2.2 *Operando* X-ray diffraction and scanning electron microscopy

To understand the structural evolution of the NMC811 material during (dis)charge, *operando* XRD measurements were collected on the four cell conditions during a full cycle, consisting of an initial charge step, followed by a discharge (Fig. S1–S4, ESI†). The unit cell parameters were determined by Rietveld refinement of the XRD patterns, and the key results are presented in Table 1 and Fig. 6. As NMC811 charges to the first plateau at 3.7 V there is a slight volume contraction consistent with removal of lithium. The volume contraction is caused by an anisotropic change in the host lattice where the *a* parameter contracts and the *c* parameter expands; this change in the lattice can be

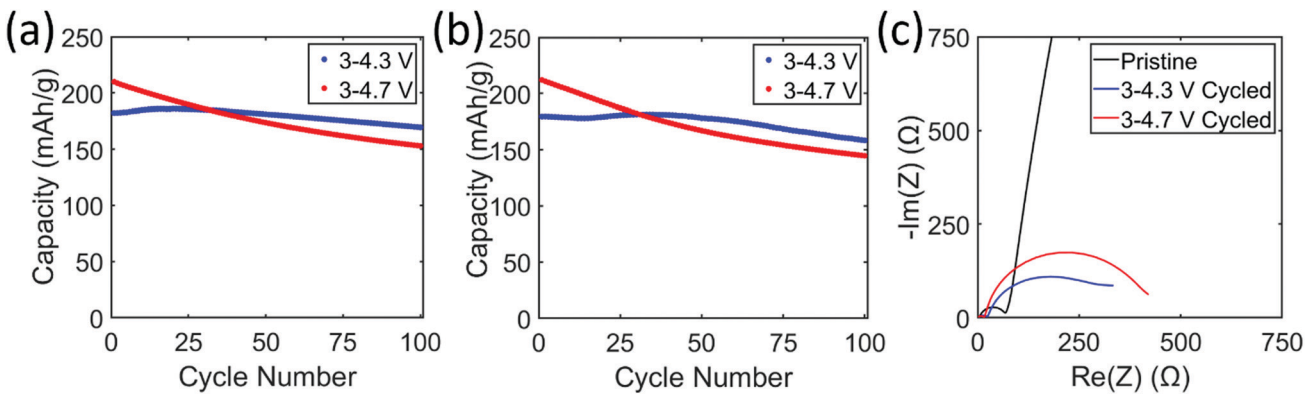

Fig. 5 (a) Representative galvanostatic cycling of Li/NMC811 coin cells, (b) representative galvanostatic cycling of Li/NMC811 pouch cells, and (c) representative EIS spectra collected on coin cells prior to cycling and cycled from 3 V to 4.3 V and 4.7 V.

Table 1 Unit cell parameters of NMC811 as determined by Rietveld refinement

	Pristine			Charged			Discharged		
Condition	a (Å)	c (Å)	V (Å^3)	a (Å)	c (Å)	V (Å^3)	a (Å)	c (Å)	V (Å^3)
4.3 Fresh	2.874	14.21	101.6	2.812	13.99	95.8	2.868	14.23	101.4
4.7 Fresh	2.872	14.19	101.4	2.812	13.57	92.9	2.868	14.22	101.3
4.3 Cycled	2.876	14.21	101.8	2.814	14.05	96.3	2.868	14.24	101.4
4.7 Cycled	2.862	14.29	101.4	2.813	13.83	94.8	2.860	14.25	101.0

described as an H1 to H2 transition, although it should be noted that these H1 and H2 phases are crystallographically equivalent in terms of space group and atomic sites and are only distinguished by their different unit cell dimensions (Fig. 6).[3,5] Upon further charging, a second plateau is reached at 4.2 V, where there is a much more significant volume contraction caused by a drastic decrease in the c parameter. This finding is consistent with an H2 → H3 transition, although it should be noted that the c parameter does not decrease as far as ≈13.7 Å – which would be expected for H3 NMC811 – suggesting that there is insufficient delithiation to fully access the volume contracted H3 phase.[3,5] Above 4.3 V, there is a sharp increase in potential up to 4.7 V. During this final part of the charging, the c parameter and volume continue to contract while the a parameter remains unchanged, showing that the H2 → H3 transition only occurs completely at the higher potential. These transitions are reversible and after discharge the material converts back to H1 NMC811.

After cycling, the NMC811 exhibits similar transitions; however, the total volume change is somewhat less consistent with the lower capacities, and therefore more limited delithiation, observed after cycling. The fact that the (3 to 4.7) V cell maintains a greater degree of phase transitions after cycling has important implications for cycling performance. For the 4.3 fresh cell, there is a 5.7% volume contraction upon charge and that change is quite similar for the 4.3 cycled cell, 5.4%. On the other hand, the 4.7 fresh cell has an 8.4% contraction which is still at 6.5% for the cycled cell. This increase in anisotropic volume change that is maintained over cycling at high potential will likely lead to particle cracking which can degrade electrical contact and lead to increased active material dissolution which will lead to capacity fade.[3,7] It is noted that although the volume change during (de)lithiation of the cycled electrodes is slightly reduced after 100x cycles, no significant changes in the lattice parameters are observed compared to the fresh electrodes. This finding is consistent with a previous study which indicated no major bulk structural changes in NMC811 electrodes after cycling 1000×, where an upper voltage cutoff of 4.5 V was used.[62]

The presence of particle cracking was confirmed by SEM measurements of NMC811 cathodes both before and after cycling from 3 V to 4.3 V and 4.7 V. High magnification images (10 000×) reveal significant particle cracking occurs primarily in the sample cycled 100 times between (3 to 4.7) V *vs.* Li/Li$^+$ (Fig. 7). Cracking appears along the grain boundaries (inter-granular fracture) of the polycrystalline micrometer sized particles, breaking the particle apart and possibly causing the smaller particles to lose contact with the conductive carbon and binder matrix. In contrast, there is minimal difference between the cathode cycled from 3 V to 4.3 V and the pristine cathode.

Notably, some recent studies have suggested that a "fatigued", underlithiated secondary NMC material can be detected upon charging after significant cycling has occurred.[17,40] These studies cite this as an additional fading mechanism caused by either kinetic limitations[40] or lattice strain at the bulk-surface interface.[17] This "fatigued" material is not detected here consistent with the lower cycle number as compared to those studies (*i.e.* the onset of the "fatigued" phase was reported at 150[40] or 300[17] cycles for the aforementioned studies which is greater than the 100 cycles experienced by NMC in this work).

2.3 *Operando* hard X-ray absorption spectroscopy

To gain additional information about the oxidation state and local environment of the transition metal cations in NMC811

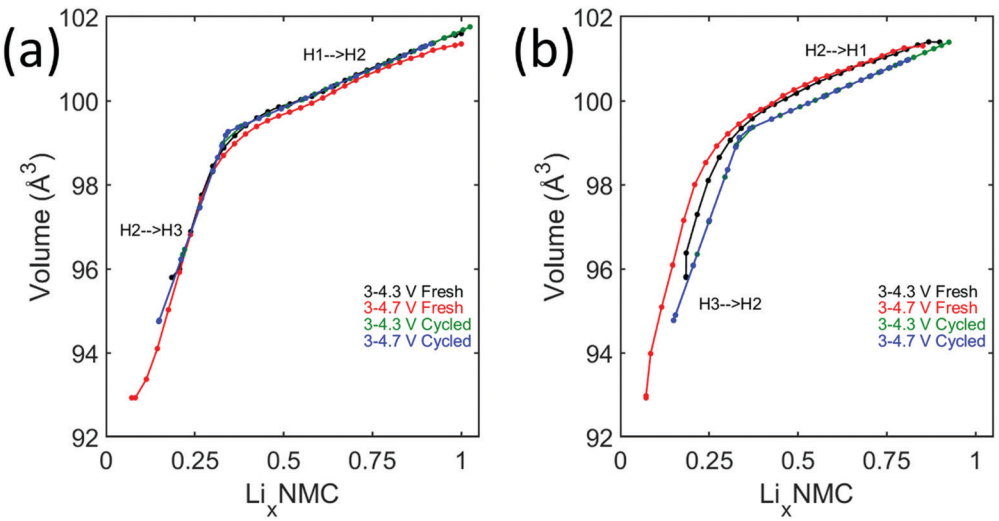

Fig. 6 Unit cell volumes determined by Rietveld refinement of the *operando* XRD patterns. (a) Patterns collected during charging and (b) patterns collected during discharging.

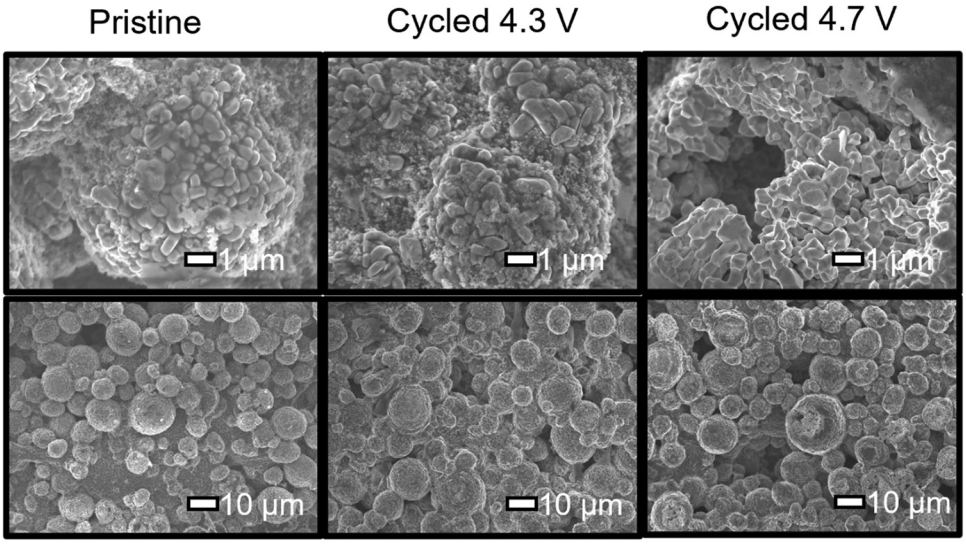

Fig. 7 SEM images at 10 000× magnification (top) and 1000× (bottom), collected top-down of NMC811 cathodes before and after cycling.

during cycling, *operando* XAS measurements were performed on the four cell types (Fig. S5–S7, ESI†). XANES on the K-edge of nickel shows a marked increase in the edge energy as the cells charge, followed by a decrease in edge energy as the cells discharge again (Fig. S5, ESI†). This suggests that nickel is oxidized significantly during charge and then reduces again during discharge. Cobalt (Fig. S7, ESI†) shows similar behavior albeit to a lesser extent implying that the cobalt is less redox-active than nickel. There is minimal edge shifting for the manganese XANES which suggests that the manganese is redox-inactive (Fig. S6, ESI†). When charged to 4.7 V, there is somewhat more oxidation of nickel than when charged to 4.3 V; there is also a more striking increase for the oxidation of cobalt at the higher potential. After cycling, the level of oxidation is more similar between potential windows consistent with the capacity fade observed for the (3 to 4.7) V cells.

To quantify the changes in oxidation state, linear combination fitting (LCF) was performed on the XANES spectra (Fig. 8 and Fig. S8, ESI†). Manganese was found to have an oxidation state of 3.9+ for all cells and states of charge which is consistent with the lack of observed edge shifting. Nickel experiences the most significant redox, oxidizing from 2.9+ to 3.9+ at 4.3 V and then reducing to 3.1+ back at 3.0 V. At 4.7 V, the oxidation state was slightly higher at the top of charge, 3.95+. After cycling, the two charging potentials lead to similar oxidation of nickel, 3.9+. Similarly, cobalt also experiences redox during cycling but to a lesser extent, 3+ to 3.5+ then to 3+ for the 4.3 fresh cell and 3+ to 3.6+ then to 3+ for 4.7 fresh cell. Likewise, the two potential windows are much more similar after cycling. The nickel oxidizes uniformly throughout the charge, while the cobalt does not begin oxidation until the end of the first plateau. This shows that delithiation leads to a conversion from H1 to H2 NMC811 characterized by oxidation of nickel followed by a conversion from H2 to H3 with further nickel oxidation and oxidation of cobalt.

To gain additional insight about the local structure of NMC811 during (de)lithiation, EXAFS data were obtained from the X-ray absorption spectra for the nickel edge as the XANES spectra show it to be the most active (Fig. S9, ESI†). Two main peaks are observed consistent with the nearest neighboring oxygen and transition metal atoms as expected for the NMC structure. During charge, these peaks shift to lower distance consistent with oxidation of the nickel which would result in shorter bond distances. During discharge, this process is reversed. Upon charge, the Ni–O peak experiences a reversible narrowing that is not seen in the other peak.

The EXAFS fit results are shown in Fig. S10 and S11 (ESI†). During charge the Ni–O and Ni–M bond distances contract by about $\approx$0.09 Å and $\approx$0.06 Å respectively consistent with oxidation of the nickel. These changes are reversible as observed from the discharging EXAFS data. Fig. S11 (ESI†) shows that there are clear changes in Debye Waller factors for the Ni–O and Ni–M distances. During charge, there is a dramatic decrease in the Ni–O path from $\approx$0.009 Å^2 to 0.004 Å^2 while the Ni–M path experiences a more moderate decrease, $\approx$0.004 Å^2 to 0.003 Å^2. When the nickel is oxidized, it changes from $Ni^{\sim 3+}$ to $Ni^{\sim 4+}$ as observed in the XANES. Ni^{3+} is d^7 and is vulnerable to Jahn–Teller distortions; this leads to the broader Ni–O peak with more disorder that is observed at the initial and discharged states.

Interestingly, although there are clear differences in the capacity retention and the bulk structure as determined by *operando* XRD, only minimal differences are noted using *operando* hard XAS between the (3 to 4.3) V and (3 to 4.7) V potential windows. Thus, sXAS measurements were performed to determine if additional differences between the two conditions could be detected.

2.4 Soft X-ray absorption spectroscopy

Ni, Mn, and Co L-edge data was recorded for pristine electrodes, and recovered electrodes after formation cycling and extended cycling to 4.3 V and 4.7 V. The Mn FY spectrum is absent due to a poor signal-to-noise ratio, attributed to self-absorption and saturation effects.[63] Across all spectra there was good agreement

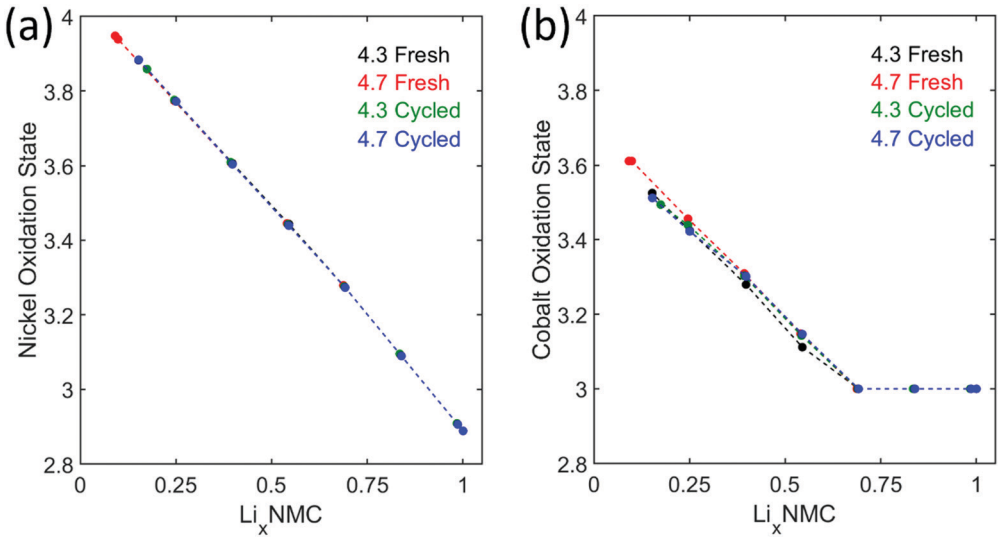

Fig. 8 Oxidation state of nickel and cobalt as determined by linear combination fitting of XANES spectra collected on charging cells. Oxidation states of (a) nickel and (b) cobalt.

for the TEY, PEY, and FY measurements, suggesting that the material's composition was consistent for the top ≈100 nm (Fig. S12, ESI†). Therefore, the TEY spectra were used for further analysis, (Fig. 9). Soft XAS and L-edge spectroscopy varies greatly by element and local atomic environment and the interested reader may look to these references for more details about Ni, Mn, Co, or L-edge spectroscopy in general.[34,35,64,65]

Significant differences in the soft XAS spectra were observed after extensive cycling, dependent on the charge voltage. The Ni L_3-edge can be described as the combination of the $L_{3,high}$ and $L_{3,low}$ peaks, with the ratio between the two peak intensities, also known as the gamma value, γ, where a drop in gamma value is correlated with a lower oxidation state.[5] For these data, the gamma values decrease from 0.579 to 0.552 and 0.327 for the pristine, 4.3 V, and 4.7 V cells, respectively (Fig. 9c) suggesting reduced Ni^{2+} on the surface of the NMC811 particles due to surface reconstruction. It is noted that the $LiNiO_2$ standard used in this study for comparison to the NMC811 data here exhibits a diminished $L_{3,high}$ peak in the Ni L-edge when compared to previous work which reported $L_{3,low}$ and $L_{3,high}$ features of roughly equal intensity,[66] with the $L_{3,high}$ peak diminishing as the lithiation content decreases.[67] This indicates slight reduction of the LNO standard; however, the gamma value of LNO is still significantly higher than the divalent NiO standard (γ = 0.54 for $LiNiO_2$, γ = 0.25 for NiO), indicating that the oxidation state of the standard is still primarily Ni^{3+}.

Furthermore, the Co and Mn spectra also show evidence of reduction. For the Mn spectra, there is a clear shift to lower eV in the L_3-edge (Fig. 9). Theoretical analyses of Mn soft XAS show that the Mn L_3-edge shifts approximately 2 eV per Mn oxidation state,[68] and analysis of Mn standards show shifts of 1.89 eV and 1.72 eV for Mn^{2+}/Mn^{3+} and Mn^{3+}/Mn^{4+} states (Fig. S13, ESI†). With extended cycling, the Mn^{4+} peak diminished as the Mn^{2+} peak increased, and the presence of both peaks suggests a mixed oxidation state (Fig. 9a). In contrast with hard XAS spectra, the soft XAS spectra show clear signatures of the different Mn oxidation states, rather than an average value.

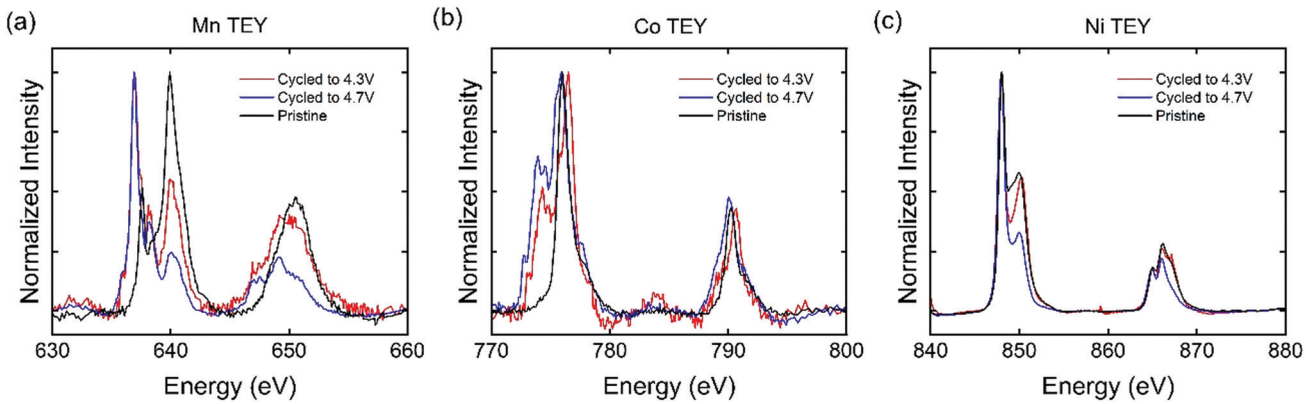

Fig. 9 Comparison of TEY for (a) Mn, (b) Co, and (c) Ni of pristine NMC811, and cycled electrodes to 4.3 V and 4.7 V.

Similarly, there was minimal change of the Co L-edge after formation suggesting no change in oxidation state.[5] However, after extended cycling, low eV features were detected that are indicative of Co^{2+} ions.[49,69]

While extremely useful for determining redox behavior, probing the transition metals alone neglects equally dynamic changes that can occur to the O^{2-} ions of NMC. Moreover, the spectral response of transition metals' L-edge is largely influenced by coordination environment, crystal field strength, and spin state. All three of these properties are highly dependent on the coordinated anions. The use of soft XAS to probe the transition metal L-edges also provides the opportunity to gain information about the O^{2-} ligands, through O K-edge measurements, with excitation energy ≈537 eV for liquid water.[37]

The O K-edge post-edge features, ≈537 eV to 545 eV, relate to the sp bonds of oxygen, while the pre-edge features, ≈525 eV to 537 eV, vary greatly by cationic species. In the case of NMC, oxygen serves as the coordinated anion for the Li, Ni, Mn, and Co cations. All these cations can influence the pre-edge features resulting in a complicated pre-edge region. The pre-edge region of NMC811 is simplified by the Ni-rich nature of the material, such that the pre-edge region can be generally indexed to nickel oxide standards (Fig. 10). The pre-edge can be indexed to four peaks, a–d, with peaks a, b, and d, being exclusive to the $LiNiO_2$ standard.[70–72] The lower excitation energy of the a and b peaks is attributed to a lower charge transfer energy due to the opening of lower valence sub-bands in the Ni^{3+} electronic structure.[73]

Electrochemically cycled samples have notably different pre-edge features than the pristine electrodes (Fig. 10e and f). The low energy a and b peaks are largely absent from the cycled electrodes suggesting more O–Ni^{2+} bond character. Moreover, the electrode recovered from the 4.3 V cycled cell shows more evidence of peak d then the electrode recovered from the 4.7 V cell, suggesting that the 4.3 V electrode has slightly more O–Ni^{3+} bond character than the 4.7 V cell (Fig. S14, ESI†). These findings further support previous claims of surface reconstruction, where O–Ni^{2+} bonds suggest the presence of lower oxidation state spinel and rocksalt phases (Fig. 4).

Taken together, the soft XAS results suggest that there is a more pronounced reduced transition metal layer on the surface of the NMC811 particles after cycling from 3 V to 4.7 V (Fig. 11). This is consistent with the formation of a reduced spinel and rocksalt surface reconstruction layer that has been implicated in capacity fading in NMC, consistent with the observed impedance rise and loss of delivered capacity (Fig. 5). These results highlight the highly useful complementary role that sXAS can play to *operando* hard X-ray characterization.

2.5 *Operando* isothermal microcalorimetry

To gain a more comprehensive understanding of battery degradation, the real-time thermal effect upon (de)lithiation of NMC811 was monitored by *operando* IMC experiments. IMC is a powerful, non-destructive tool to capture the instantaneous heat flow released from a cycling battery with ultra-high precision.[74,75] The IMC tests were performed with coin-type

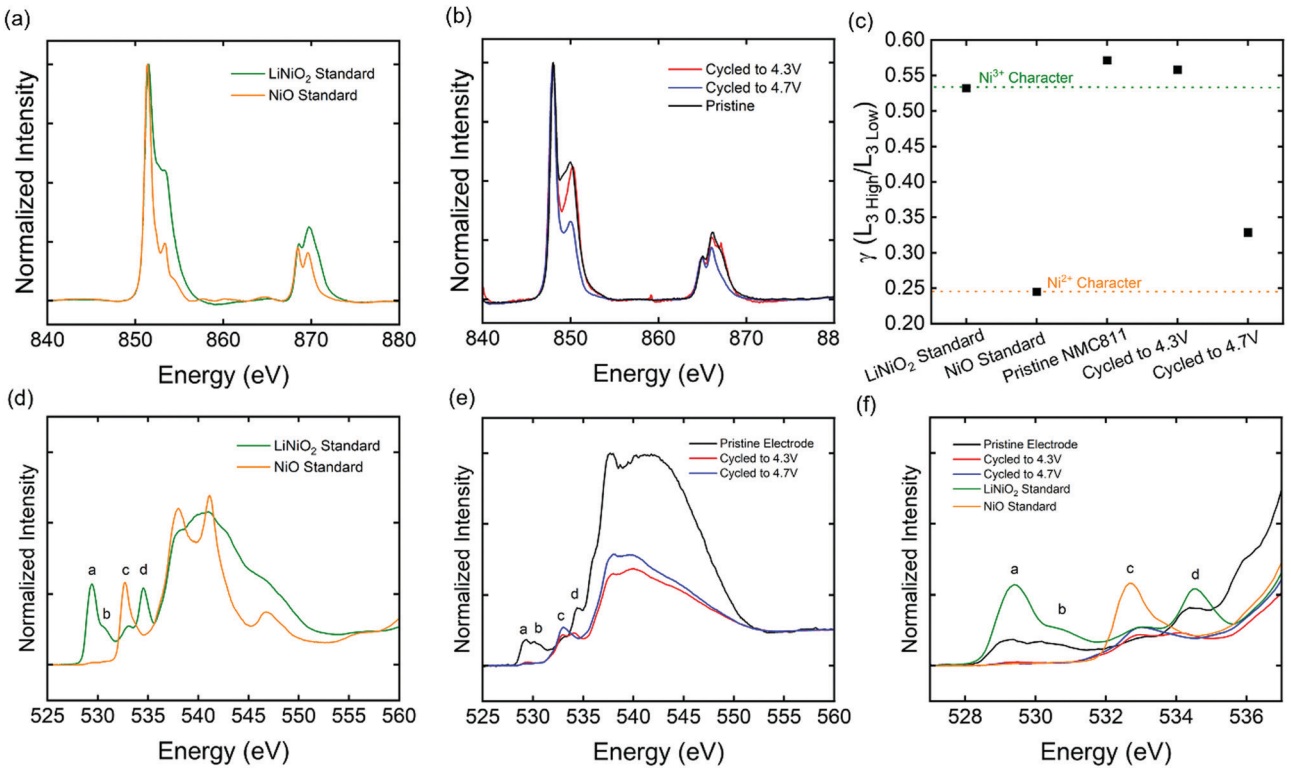

Fig. 10 (a) TEY Ni L-edge of the Ni standards, (b) NMC811 electrodes, (c) gamma values from the Ni L-edge. (d) TEY O K-edge of the Ni standards (e) NMC811 electrodes, and (f) the pre-edge features.

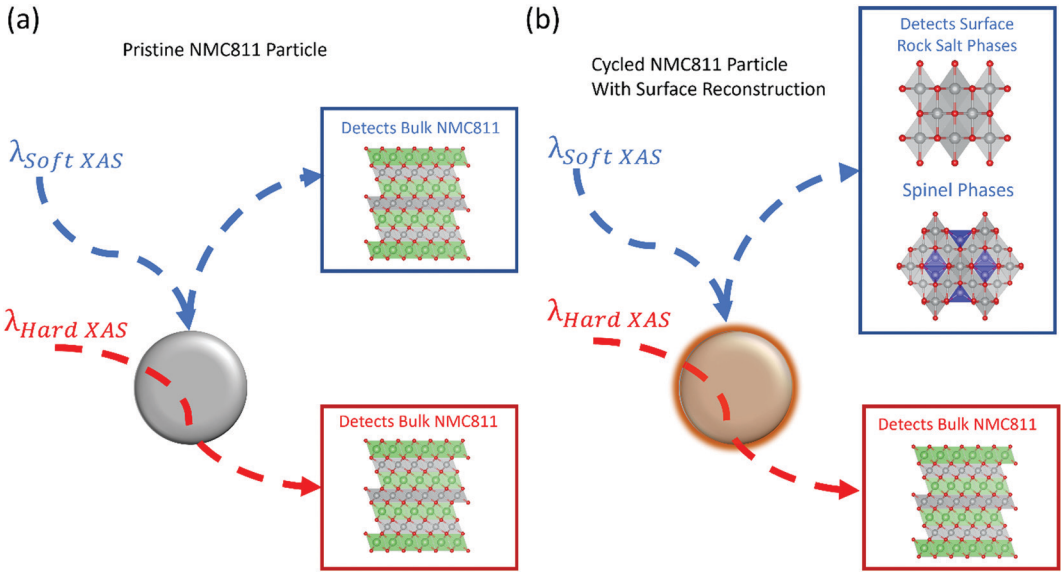

Fig. 11 Conceptual schematic of hard and soft X-rays interacting with (a) a pristine NMC811 particle and (b) a NMC811 particle after extended cycling.

Li/NMC811 cells cycled with two upper voltage limits, 4.3 V and 4.7 V (Fig. S15, ESI†). Two cells were successively cycled for four cycles at C-rates of C/10, C/5, C/2, and 1C following formation cycling. Independent of current rate, the voltage hysteresis enclosed by the charge and discharge electrochemical profiles is significantly expanded in the cell cycled in 3–4.7 V (Fig. 12b) compared to that of the cell cycled with a moderate voltage limit of 4.3 V (Fig. 12a). The area of the voltage hysteresis is an effective indicator of electrochemical inefficiency.[76] The enlarged voltage hysteresis physically represents an increased amount of electrical energy loss, and thermal dissipation could be a major contributing factor to this energy loss.[32] For the cell cycled in 3–4.7 V, an intense heat flow spike could be spotted at a high state-of-charge (>4.3 V) at every C-rate (Fig. S15b, ESI†). Representative heat flow curves during the charge step at C/5 were demonstrated in Fig. 12c, where a ~5× heat flow surge occurred at the end of charge in the high-voltage area. The total heat generated throughout a complete charge–discharge cycle was calculated based on eqn (1) and shown in Fig. 12d.

$$Q = \oint \dot{q}\,\mathrm{d}t \tag{1}$$

The thermal dissipation generated from the cell cycled at 3–4.7 V was almost double compared to its counterpart cycled at 3–4.3 V, regardless of the current rate from C/10 to 1C. Therefore, the high voltage charge to 4.7 V on Li/NMC811 cells would cause a significant rise of heat dissipation and lower the energy conversion efficiency from the stored chemical energy to useful electrical work through thermal energy waste.

The heat dissipation from electrochemical cells upon cycling is closely correlated with the structural change of the electrode materials.[77] However, thermodynamic parameters of $Li_xNi_{0.8}Mn_{0.1}Co_{0.1}O_2$ were commonly studied in cases of high-temperature-induced decomposition[77,78] rather than electrochemical (de)lithiation at room temperature. Herein, the thermodynamic enthalpy change upon solid-state phase transitions was also investigated using the IMC data.

A representative electrochemical profile and its corresponding differential capacity ($\mathrm{d}Q/\mathrm{d}V$) plot are shown in Fig. 13a. In the $\mathrm{d}Q/\mathrm{d}V$ plot, two distinct peaks at ~3.75 V and ~4.20 V are observed that are associated with the H1 → H2 and H2 → H3 transitions, respectively. The enthalpy potential upon the delithiation (charge) of NMC811 was determined with the IMC data based on eqn (2),[32] where V and I are loaded voltage and current of the cycling cell and $\dot{q}$ is the instantaneous heat flow.

$$U_H = V - \frac{\dot{q}}{I} \tag{2}$$

The calculated enthalpy potential (U_H) curves at different C-rates varying from C/10, C5, and C/2 were superimposed on each other (Fig. 13b), which indicates that the enthalpy potential is a thermodynamic parameter and independent of kinetics. The enthalpy values were further calculated by integrating the U_H (in units of volts) over capacity (in units of mA h g^{-1}) in areas corresponding to multiple-step structural evolution processes (Fig. 13c).[79] Calculation results are presented in Table 2.

As revealed in Table 2, when delivering a unit capacity, the occurrence of the H2 and H3 phases successively contributed to increased reaction heat (ΔH). Therefore, regardless of the applied current rates, an in-depth delithiation accompanying the presence of the H3 phase results in an enlarged heat generation from thermodynamics. The U_H plots calculated from cells that were charged to 4.7 V at different C-rates were illustrated in Fig. S16 (ESI†). Similar to what was demonstrated in Fig. 13b, in most of state-of-charge (SoC) ranges, the U_H curves corresponding to charge processes to 4.7 V at C/10, C/5, C/2 were also overlaid with each other. Nevertheless, local discrepancies among curves could be observed in the

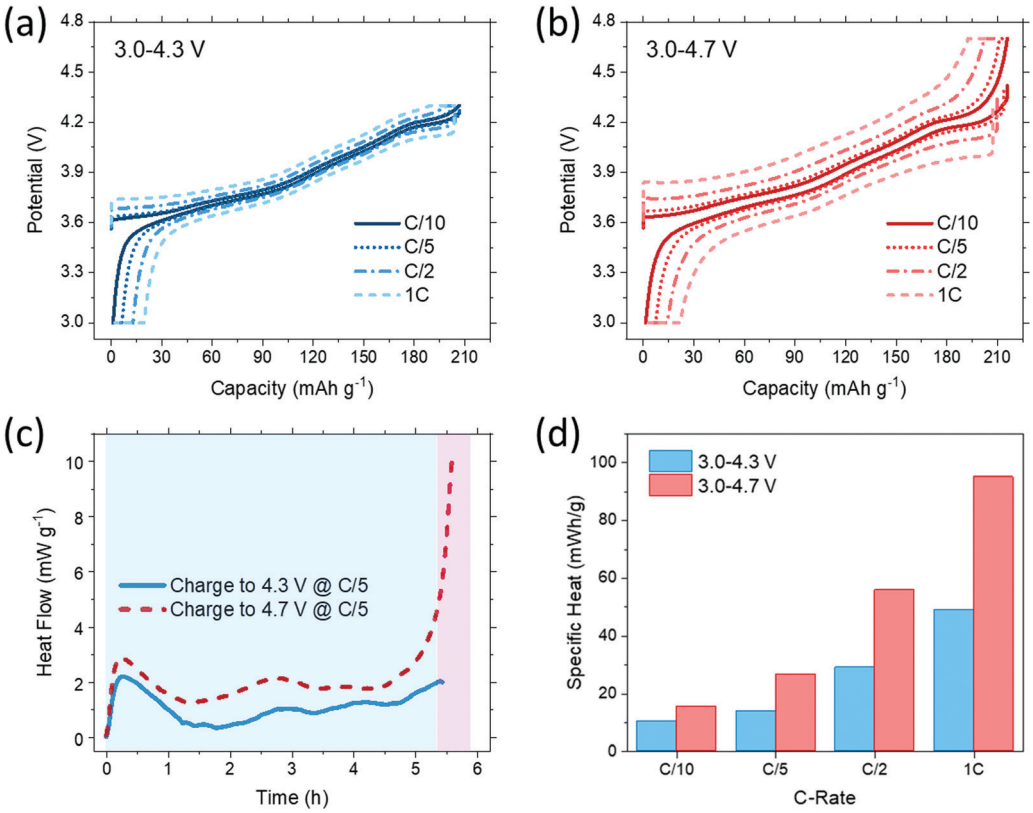

Fig. 12 Galvanostatic cycling of Li/NMC811 coin cells in the *operando* IMC test with a charge limit of (a) 4.3 V and (b) 4.7 V. (c) Representative heat flow curves of cells charged to 4.3 V and 4.7 V at C/5. (d) The total heat generated throughout a complete charge-discharge cycle at different C-rates.

high-voltage area (Fig. S16, ESI†), which indicates path-dependent thermodynamics locally at high voltage. The path-dependent thermodynamic path, suggesting thermodynamically irreversible electrochemical processes, could be an origin of voltage hysteresis triggering energy conversion inefficiency.[32,76] Additionally, parasitic reactions, including the surface reconstruction revealed by the sXAS, at high voltages can be another critical contributing factor to the significantly increased heat dissipation. In summary, high-voltage and high SoC charge (delithiation) could cause irreversible energy loss through thermal dissipation due to thermodynamic factors. Even in low C-rate cycling, this part of energy loss cannot be recovered by subsequent recharge and thereby contributes to the rapid fading of energy storage capacity in the long term.

2.6 Future outlook

The combined use of hard and soft XAS techniques provides a comprehensive view of the dynamic structural and electronic changes resulting in capacity fade of Ni-rich NMC materials. For hard XAS measurements, advances in cell design have enabled *operando* measurements on extensively cycled batteries, with the case study presented here as a relevant example. This type of methodology permits correlation of oxidation state, local and long-range structural information with changes in electrochemical behavior after battery aging. At the same time, this approach eliminates possible issues with cell-to-cell consistency, electrode shorting or contamination that can occur during destructive analysis of batteries for *ex situ* measurement.

Future *operando* hard X-ray studies of NMC degradation mechanisms should move towards measurement of aged cells in lithium limited (full cell) configurations to approximate the conditions of commercial graphite/NMC batteries more closely. For soft XAS, the complex and nuanced nature of transition metal L-edge and O K-edge have resulted in no clear-cut best practices, especially in the battery field. Experimentally, taking inspiration from hard XAS, there is a push towards *operando* soft XAS, where numerous logistical challenges are being met through a combination of beamline improvements and modified cell designs.[80] For example, recent studies suggest that the formation of oxygenated electrolyte decomposition products on the surface of NMC materials are significant and must be considered during assessment of O K-edge data.[18] Additionally, the improvement and growing accessibility of computational modeling will also continue to inform both types of characterization techniques and should be included whenever viable.

Beyond the probing of electrochemical thermodynamics, future *operando* IMC investigations should expand the research focus to the understanding of the impacts of electrochemical kinetics to the thermal behavior upon NMC811 (de)lithiation. The majority of heat dissipation from battery cycling comes from the ohmic heat which is numerically proportional to the current squared. Therefore, fast charging ($\geq$4C) is expected to simultaneously bring significant heat dissipation which can be

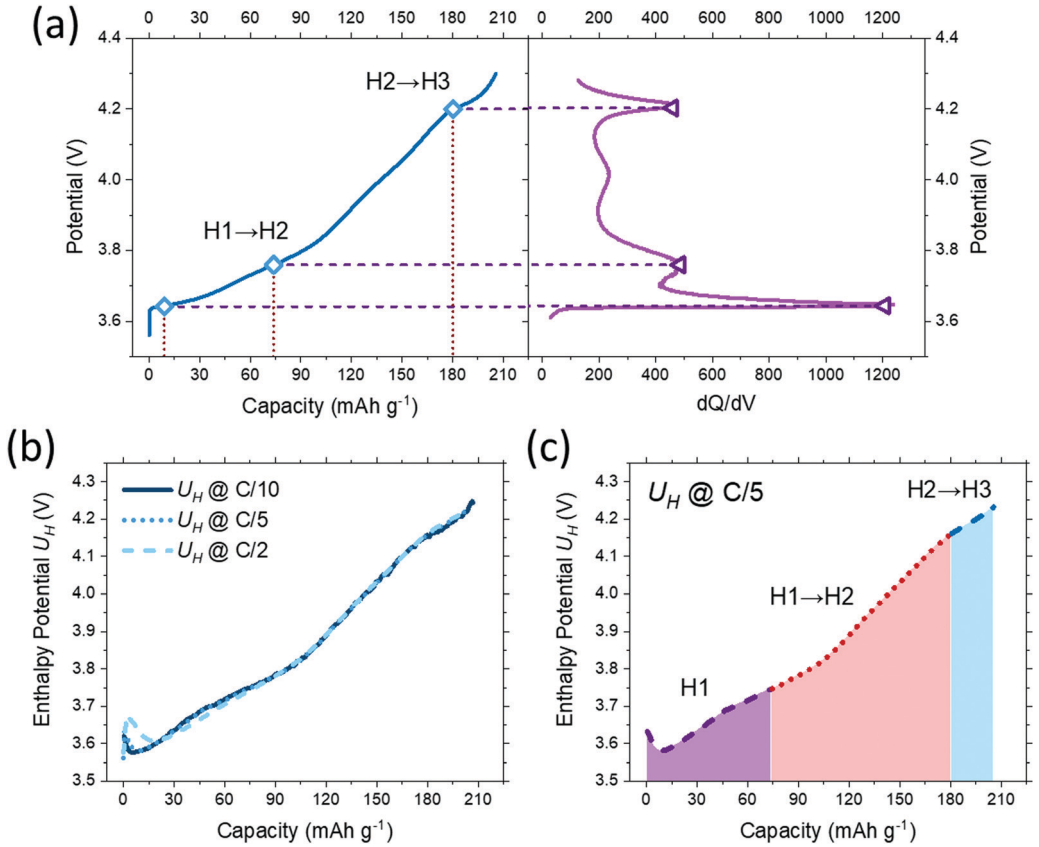

Fig. 13 (a) Electrochemical profile and its corresponding differential capacity (dQ/dV) plot of cells cycled in the IMC test (charge to 4.3 V at C/5). (b) The enthalpy potential upon charge to 4.3 V at C-rates of C/10, C/5, and C/2. (c) The enthalpy calculation method in multiple-step structural evolution processes.

Table 2 Capacity-normalized enthalpy values upon NMC811 delithiation

	Enthalpy (J g^{-1})	Capacity (mA h g^{-1})	Capacity-normalized enthalpy (J mA^{-1} h^{-1})
H1	972.8	73.8	13.2
H1 → H2	1490.6	106.4	14.0
H2 → H3	372.1	25.2	14.8

a concern from the perspectives of full energy utilization and safe operation. A comprehensive understanding of real-time thermal features during fast charging is essential to address unanswered questions and navigate methods to control excess heat release.

3 Conclusions

NMC, especially Ni-rich NMC, is an immensely important cathode for Li-ion battery systems; however, its capacity must be limited to well below its theoretical value to preserve cycling stability. To utilize a greater portion of that high theoretical capacity the underlying causes of fading in the NMC system must be first understood. Substantial progress has been made to this end using hard X-ray characterization, in particular when conducted *operando*, to track the evolution of structure, oxidation state, and local coordination environment during NMC (de)lithiation. Studies have demonstrated that NMC undergoes significant anisotropic lattice changes during cycling that can cause repeated volume changes on both the crystallite and particle level. These changes can cause particle fracture which in turn can cause capacity fading due to loss of electrical contact, loss of active material, and increased cathode-electrolyte interface reactions. Critically, the evolution of the NMC surface has also been implicated in capacity fading, where reduced spinel and rocksalt NMC phases form on the particle surface due to loss of oxygen during cycling. Here sXAS presents an avenue for more complete understanding through the acquisition of detailed information about the oxidation state and coordination environment on the particle surface.

To illustrate the utility of using X-ray probes to characterize mechanisms of capacity fade in NMC811, a case study is presented in which the material was cycled from 3.0 V to upper voltage limits of 4.3 V or 4.7 V. The system was characterized with *operando* XRD and XAS over extended cycling which allowed for the study of fading mechanisms as the fading occurred in real time. XRD and complementary SEM showed that the high voltage limit led to increased structural distortions and particle fracture; however, *operando* hard XAS revealed limited additional differences between the two voltage windows. Additional *ex situ*

sXAS measurements were collected and revealed significant surface reduction specifically after cycling at 4.7 V consistent with a more substantial surface reconstruction layer and thus the observed capacity fade. Furthermore, *operando* isothermal microcalorimetry reveals a substantial rise in heat dissipation coupled with lower efficiency of energy conversion from the stored chemical energy to useful electrical work, suggesting that greater levels of capacity fade observed during high voltage charging may be triggered by greater thermal energy waste. Overall, these results showcase the importance of comprehensive X-ray characterization and microcalorimetric techniques to obtain a full picture of the causes of capacity fading in the NMC materials.

Conflicts of interest

There are no conflicts of interest to declare.

Acknowledgements

The authors acknowledge Mercedes-Benz Research and Development North America (MBRDNA) for supporting mechanistic studies relevant to NMC. The work to characterize resiliency of the battery relates to Department of Navy award N00014-20-1-2858 issued by the Office of Naval Research (ONR). The United States Government has a royalty-free license throughout the world in all copyrightable material contained herein. Development of the pouch cell assembly and testing methodology was supported as part of the Center for Mesoscale Transport Properties, an Energy Frontier Research Center funded by the U.S. Department of Energy, Office of Science, Basic Energy Sciences, under award #DE-SC0012673. The pouch cell assembly line was supported under award 75039 from the New York State Energy Research and Development Authority (NYSERDA) and award 76890 from the New York State Department of Economic Development (DED), which were provided as matching funds to the Center of Mesoscale Transport Properties. NYSERDA has not reviewed the information contained herein, and the opinions expressed do not necessarily reflect those of NYSERDA, or the State of New York. Any opinions, findings, and conclusions, or recommendations expressed are those of the author(s) and do not necessarily reflect the views of the ONR, DED or the federal government. E. S. T. acknowledges support as the William and Jane Knapp Chair in Energy and the Environment. This research used resources of beamline 7-BM Quick X-ray Absorption and Scattering (QAS) and beamline 7-ID-1 Spectroscopy Soft and Tender (SST-1) of the National Synchrotron Light Source II, a U.S. Department of Energy (DOE), Office of Science User Facility operated for the DOE Office of Science by Brookhaven National Laboratory under contract no. DE-SC0012704.

References

1 F. Schipper, E. M. Erickson, C. Erk, J.-Y. Shin, F. F. Chesneau and D. Aurbach, *J. Electrochem. Soc.*, 2017, **164**, A6220–A6228.
2 C. D. Quilty, G. P. Wheeler, L. Wang, A. H. McCarthy, S. Yan, K. R. Tallman, M. R. Dunkin, X. Tong, S. Ehrlich, L. Ma, K. J. Takeuchi, E. S. Takeuchi, D. C. Bock and A. C. Marschilok, *ACS Appl. Mater. Interfaces*, 2021, **13**, 50920–50935.
3 C. D. Quilty, D. C. Bock, S. Yan, K. J. Takeuchi, E. S. Takeuchi and A. C. Marschilok, *J. Phys. Chem. C*, 2020, **124**, 8119–8128.
4 K. R. Tallman, G. P. Wheeler, C. J. Kern, E. Stavitski, X. Tong, K. J. Takeuchi, A. C. Marschilok, D. C. Bock and E. S. Takeuchi, *J. Phys. Chem. C*, 2020, **125**(1), 58–73.
5 C. Tian, D. Nordlund, H. L. Xin, Y. Xu, Y. Liu, D. Sokaras, F. Lin and M. M. Doeff, *J. Electrochem. Soc.*, 2018, **165**, A696–A704.
6 C. Tian, F. Lin and M. M. Doeff, *Acc. Chem. Res.*, 2018, **51**, 89–96.
7 M. D. Radin, S. Hy, M. Sina, C. Fang, H. Liu, J. Vinckeviciute, M. Zhang, M. S. Whittingham, Y. S. Meng and A. Van der Ven, *Adv. Energy Mater.*, 2017, **7**, 1602888.
8 D. Andre, S.-J. Kim, P. Lamp, S. F. Lux, F. Maglia, O. Paschos and B. Stiaszny, *J. Mater. Chem. A*, 2015, **3**, 6709–6732.
9 S. C. Yin, Y. H. Rho, I. Swainson and L. F. Nazar, *Chem. Mater.*, 2006, **18**, 1901–1910.
10 A. Manthiram, J. C. Knight, S.-T. Myung, S.-M. Oh and Y.-K. Sun, *Adv. Energy Mater.*, 2016, **6**, 1501010.
11 S.-K. Jung, H. Gwon, J. Hong, K.-Y. Park, D.-H. Seo, H. Kim, J. Hyun, W. Yang and K. Kang, *Adv. Energy Mater.*, 2014, **4**, 1300787.
12 S.-M. Bak, E. Hu, Y. Zhou, X. Yu, S. D. Senanayake, S.-J. Cho, K.-B. Kim, K. Y. Chung, X.-Q. Yang and K.-W. Nam, *ACS Appl. Mater. Interfaces*, 2014, **6**, 22594–22601.
13 A. O. Kondrakov, H. Gesswein, K. Galdina, L. de Biasi, V. Meded, E. O. Filatova, G. Schumacher, W. Wenzel, P. Hartmann, T. Brezesinski and J. Janek, *J. Phys. Chem. C*, 2017, **121**, 24381–24388.
14 A. O. Kondrakov, A. Schmidt, J. Xu, H. Gesswein, R. Moenig, P. Hartmann, H. Sommer, T. Brezesinski and J. Janek, *J. Phys. Chem. C*, 2017, **121**, 3286–3294.
15 F. Friedrich, B. Strehle, A. T. S. Freiberg, K. Kleiner, S. J. Day, C. Erk, M. Piana and H. A. Gasteiger, *J. Electrochem. Soc.*, 2019, **166**, A3760–A3774.
16 H. Li, J. Li, X. Ma and J. R. Dahn, *J. Electrochem. Soc.*, 2018, **165**, A1038–A1045.
17 X. Li, A. Gao, Z. Tang, F. Meng, T. Shang, S. Guo, J. Ding, Y. Luo, D. Xiao, X. Wang, D. Su, Q. Zhang and L. Gu, *Adv. Funct. Mater.*, 2021, **31**, 2010291.
18 Y. Yu, P. Karayaylali, L. Giordano, J. Corchado-Garcia, J. Hwang, D. Sokaras, F. Maglia, R. Jung, F. S. Gittleson and Y. Shao-Horn, *ACS Appl. Mater. Interfaces*, 2020, **12**, 55865–55875.
19 E. R. Logan, H. Hebecker, X. Ma, J. Quinn, Y. HyeJeong, S. Kumakura, J. Paulsen and J. R. Dahn, *J. Electrochem. Soc.*, 2020, **167**, 060530.
20 T. M. M. Heenan, A. Wade, C. Tan, J. E. Parker, D. Matras, A. S. Leach, J. B. Robinson, A. Llewellyn, A. Dimitrijevic, R. Jervis, P. D. Quinn, D. J. L. Brett and P. R. Shearing, *Adv. Energy Mater.*, 2020, **10**, 2002655.
21 K. Marker, P. J. Reeves, C. Xu, K. J. Griffith and C. P. Grey, *Chem. Mater.*, 2019, **31**, 2545–2554.

22 J. Zheng, T. Liu, Z. Hu, Y. Wei, X. Song, Y. Ren, W. Wang, M. Rao, Y. Lin, Z. Chen, J. Lu, C. Wang, K. Amine and F. Pan, *J. Am. Chem. Soc.*, 2016, **138**, 13326–13334.
23 Y. W. Tsai, J. F. Lee, D. G. Liu and B. J. Hwang, *J. Mater. Chem.*, 2004, **14**, 958–965.
24 M. Balasubramanian, X. Sun, X. Q. Yang and J. McBreen, *J. Electrochem. Soc.*, 2000, **147**, 2903–2909.
25 A. Rougier and C. Delmas, *Solid State Commun.*, 1995, **94**, 123–127.
26 A. N. Mansour, J. McBreen and C. A. Melendres, *J. Electrochem. Soc.*, 1999, **146**, 2799–2809.
27 I. Nakai and T. Nakagome, *Electrochem. Solid-State Lett.*, 1998, **1**, 259–261.
28 S. Sicolo, M. Mock, M. Bianchini and K. Albe, *Chem. Mater.*, 2020, **32**, 10096–10103.
29 D. Goonetilleke, N. Sharma, W. K. Pang, V. K. Peterson, R. Petibon, J. Li and J. R. Dahn, *Chem. Mater.*, 2019, **31**, 376–386.
30 A. K. C. Estandarte, J. Diao, A. V. Llewellyn, A. Jnawali, T. M. M. Heenan, S. R. Daemi, J. J. Bailey, S. Cipiccia, D. Batey, X. Shi, C. Rau, D. J. L. Brett, R. Jervis, I. K. Robinson and P. R. Shearing, *ACS Nano*, 2021, **15**, 1321–1330.
31 C. Mao, R. E. Ruther, L. Geng, Z. Li, D. N. Leonard, H. M. Meyer, R. L. Sacci and D. L. Wood, *ACS Appl. Mater. Interfaces*, 2019, **11**, 43235–43243.
32 W. Li, L. M. Housel, G. P. Wheeler, D. C. Bock, K. J. Takeuchi, E. S. Takeuchi and A. C. Marschilok, *ACS Appl. Energy Mater.*, 2021, **4**, 12067–12073.
33 M. L. Baker, M. W. Mara, J. J. Yan, K. O. Hodgson, B. Hedman and E. I. Solomon, *Coord. Chem. Rev.*, 2017, **345**, 182–208.
34 F. d. Groot, *Coord. Chem. Rev.*, 2005, **249**, 31–63.
35 G. V. D. Laan and I. W. Kirkman, *J. Phys.: Condens. Matter*, 1992, **4**, 4189–4204.
36 J. W. Smith and R. J. Saykally, *Chem. Rev.*, 2017, **117**, 13909–13934.
37 S. Myneni, Y. Luo, L. Å. Näslund, M. Cavalleri, L. Ojamäe, H. Ogasawara, A. Pelmenschikov, P. Wernet, P. Väterlein, C. Heske, Z. Hussain, L. G. M. Pettersson and A. Nilsson, *J. Phys.: Condens. Matter*, 2002, **14**, L213–L219.
38 G.-L. Xu, Q. Liu, K. K. S. Lau, Y. Liu, X. Liu, H. Gao, X. Zhou, M. Zhuang, Y. Ren, J. Li, M. Shao, M. Ouyang, F. Pan, Z. Chen, K. Amine and G. Chen, *Nat. Energy*, 2019, **4**, 484–494.
39 S. Neudeck, A. Mazilkin, C. Reitz, P. Hartmann, J. Janek and T. Brezesinski, *Sci. Rep.*, 2019, **9**, 5328.
40 S. Schweidler, L. de Biasi, G. Garcia, A. Mazilkin, P. Hartmann, T. Brezesinski and J. Janek, *ACS Appl. Energy Mater.*, 2019, **2**(10), 7375–7384.
41 S. Schweidler, L. de Biasi, P. Hartmann, T. Brezesinski and J. Janek, *ACS Appl. Energy Mater.*, 2020, **3**, 2821–2827.
42 W.-S. Yoon, M. Balasubramanian, K. Y. Chung, X.-Q. Yang, J. McBreen, C. P. Grey and D. A. Fischer, *J. Am. Chem. Soc.*, 2005, **127**, 17479–17487.
43 K. Marker, C. Xu and C. P. Grey, *J. Am. Chem. Soc.*, 2020, **142**, 17447–17456.
44 K. Min, C. Jung, D.-S. Ko, K. Kim, J. Jang, E. Cho and K. Park, *ACS Appl. Mater. Interfaces*, 2018, **10**, 20599–20610.
45 G. Qian, Y. Zhang, L. Li, R. Zhang, J. Xu, Z. Cheng, S. Xie, H. Wang, Q. Rao, Y. He, Y. Shen, L. Chen, M. Tang and Z.-F. Ma, *Energy Storage Mater.*, 2020, **27**, 140–149.
46 X. Cheng, J. Zheng, J. Lu, Y. Li, P. Yan and Y. Zhang, *Nano Energy*, 2019, **62**, 30–37.
47 H.-H. Ryu, K.-J. Park, C. S. Yoon and Y.-K. Sun, *Chem. Mater.*, 2018, **30**, 1155–1163.
48 Z. Xu, M. M. Rahman, L. Mu, Y. Liu and F. Lin, *J. Mater. Chem. A*, 2018, **6**, 21859–21884.
49 F. Lin, I. M. Markus, D. Nordlund, T.-C. Weng, M. D. Asta, H. L. Xin and M. M. Doeff, *Nat. Commun.*, 2014, **5**, 3529.
50 L. Geng, J. Liu, D. L. Wood, Y. Qin, W. Lu, C. J. Jafta, Y. Bai and I. Belharouak, *ACS Appl. Energy Mater.*, 2020, **3**, 7058–7065.
51 X. Liu and C. T. Prewitt, *Phys. Chem. Miner.*, 1990, **17**, 168–172.
52 A. Leineweber, H. Jacobs and S. Hull, *Inorg. Chem.*, 2001, **40**, 5818–5822.
53 P. Bleuet, E. Welcomme, E. Dooryhée, J. Susini, J.-L. Hodeau and P. Walter, *Nat. Mater.*, 2008, **7**, 468–472.
54 H. Liu, S. Kazemiabnavi, A. Grenier, G. Vaughan, M. Di Michiel, B. J. Polzin, K. Thornton, K. W. Chapman and P. J. Chupas, *ACS Appl. Mater. Interfaces*, 2019, **11**, 18386–18394.
55 D. P. Finegan, A. Vamvakeros, C. Tan, T. M. M. Heenan, S. R. Daemi, N. Seitzman, M. Di Michiel, S. Jacques, A. M. Beale, D. J. L. Brett, P. R. Shearing and K. Smith, *Nat. Commun.*, 2020, **11**, 631.
56 S. R. Daemi, C. Tan, A. Vamvakeros, T. M. M. Heenan, D. P. Finegan, M. Di Michiel, A. M. Beale, J. Cookson, E. Petrucco, J. S. Weaving, S. Jacques, R. Jervis, D. J. L. Brett and P. R. Shearing, *Phys. Chem. Chem. Phys.*, 2020, **22**, 17814–17823.
57 S. Spence, W.-K. Lee, F. Lin and X. Xiao, *Nanotechnology*, 2021, **32**, 442003.
58 Y. Mao, X. Wang, S. Xia, K. Zhang, C. Wei, S. Bak, Z. Shadike, X. Liu, Y. Yang, R. Xu, P. Pianetta, S. Ermon, E. Stavitski, K. Zhao, Z. Xu, F. Lin, X.-Q. Yang, E. Hu and Y. Liu, *Adv. Funct. Mater.*, 2019, **29**, 1900247.
59 Y. Yang, R. Xu, K. Zhang, S.-J. Lee, L. Mu, P. Liu, C. K. Waters, S. Spence, Z. Xu, C. Wei, D. J. Kautz, Q. Yuan, Y. Dong, Y.-S. Yu, X. Xiao, H.-K. Lee, P. Pianetta, P. Cloetens, J.-S. Lee, K. Zhao, F. Lin and Y. Liu, *Adv. Energy Mater.*, 2019, **9**, 1900674.
60 C. Tian, Y. Xu, D. Nordlund, F. Lin, J. Liu, Z. Sun, Y. Liu and M. Doeff, *Joule*, 2018, **2**, 464–477.
61 Z. Xu, Z. Jiang, C. Kuai, R. Xu, C. Qin, Y. Zhang, M. M. Rahman, C. Wei, D. Nordlund, C.-J. Sun, X. Xiao, X.-W. Du, K. Zhao, P. Yan, Y. Liu and F. Lin, *Nat. Commun.*, 2020, **11**, 83.
62 F. Friedrich, B. Strehle, A. T. S. Freiberg, K. Kleiner, S. J. Day, C. Erk, M. Piana and H. A. Gasteiger, *J. Electrochem. Soc.*, 2019, **166**, A3760–A3774.
63 D. Asakura, E. Hosono, Y. Nanba, H. Zhou, J. Okabayashi, C. Ban, P.-A. Glans, J. Guo, T. Mizokawa, G. Chen,

A. J. Achkar, D. G. Hawthron, T. Z. Regier and H. Wadati, *AIP Adv.*, 2016, **6**, 035105.
64 M. U. Delgado-Jaime, K. Zhang, J. Vura-Weis and F. M. F. de Groot, *J. Synchrotron Radiat.*, 2016, **23**, 1600–5775.
65 F. De Groot and A. Kotani, *Core level spectroscopy of solids*, CRC press, 2008.
66 M. Bianchini, A. Schiele, S. Schweidler, S. Sicolo, F. Fauth, E. Suard, S. Indris, A. Mazilkin, P. Nagel, S. Schuppler, M. Merz, P. Hartmann, T. Brezesinski and J. Janek, *Chem. Mater.*, 2020, **32**, 9211–9227.
67 W.-S. Yoon, K. Y. Chung, J. McBreen, D. A. Fischer and X.-Q. Yang, *J. Power Sources*, 2006, **163**, 234–237.
68 H. Wang, S. Friedrich, L. Li, Z. Mao, P. Ge, M. Balasubramanian and D. S. Patil, *Phys. Chem. Chem. Phys.*, 2018, **20**, 8166–8176.
69 D. K. Bora, X. Cheng, M. Kapilashrami, P. A. Glans, Y. Luo and J. H. Guo, *J. Synchrotron Radiat.*, 2015, **22**, 1450–1458.
70 Y. Uchimoto, H. Sawada and T. Yao, *J. Power Sources*, 2001, **97-98**, 326–327.
71 M. G. Kim, N. E. Sung, H. J. Shin, N. S. Shin, K. S. Ryu and C. H. Yo, *Electrochim. Acta*, 2004, **50**, 501–504.
72 L. A. Grunes, R. D. Leapman, C. N. Wilker, R. Hoffmann and A. B. Kunz, *Phys. Rev. B: Condens. Matter Mater. Phys.*, 1982, **25**, 7157–7173.
73 F. Frati, M. O. J. Y. Hunault and F. M. F. de Groot, *Chem. Rev.*, 2020, **120**, 4056–4110.
74 L. M. Housel, W. Li, C. D. Quilty, M. N. Vila, L. Wang, C. R. Tang, D. C. Bock, Q. Wu, X. Tong and A. R. Head, *ACS Appl. Mater. Interfaces*, 2019, **11**, 37567–37577.
75 M. M. Huie, D. C. Bock, L. Wang, A. C. Marschilok, K. J. Takeuchi and E. S. Takeuchi, *J. Phys. Chem. C*, 2018, **122**, 10316–10326.
76 G. Assat, S. L. Glazier, C. Delacourt and J.-M. Tarascon, *Nat. Energy*, 2019, **4**, 647–656.
77 Y. Wang, D. Ren, X. Feng, L. Wang and M. Ouyang, *J. Power Sources*, 2021, **514**, 230582.
78 Y. Wang, D. Ren, X. Feng, L. Wang and M. Ouyang, *Appl. Energy*, 2022, **306**, 117943.
79 V. L. Chevrier, Z. Yan, S. L. Glazier, M. N. Obrovac and L. J. Krause, *J. Electrochem. Soc.*, 2021, **168**, 030504.
80 F. Yang, X. Feng, Y.-S. Liu, L. C. Kao, P.-A. Glans, W. Yang and J. Guo, *Energy Environ. Mater.*, 2021, **4**, 139–157.